Post-depositional manganese mobilization during the last glacial period in sediments of the eastern Clarion-Clipperton Zone, Pacific Ocean

Jessica B. Volz [a],[*], Bo Liu [a], Male Köster [a], Susann Henkel [a], Andrea Koschinsky [b], Sabine Kasten [a],[c]

[a] Alfred Wegener Institute Helmholtz Centre for Polar and Marine Research, Bremerhaven, Germany
[b] Jacobs University Bremen, Department of Physics and Earth Sciences, Bremen, Germany
[c] University of Bremen, Faculty of Geosciences, Klagenfurter Strasse, Bremen, Germany

A B S T R A C T

Numerous studies have provided compelling evidence that the Pacific Ocean has experienced substantial glacial/interglacial changes in bottom-water oxygenation associated with enhanced carbon dioxide storage in the glacial deep ocean. Under postulated low glacial bottom-water oxygen concentrations (O_2^{bw}), redox zonation, biogeochemical processes and element fluxes in the sediments must have been distinctively different during the last glacial period (LGP) compared to current well-oxygenated conditions.

In this study, we have investigated six sites situated in various European contract areas for the exploration of polymetallic nodules within the Clarion-Clipperton Zone (CCZ) in the NE Pacific and one site located in a protected Area of Particular Environmental Interest (APEI3) north of the CCZ. We found bulk sediment Mn maxima of up to 1 wt% in the upper oxic 10 cm of the sediments at all sites except for the APEI3 site. The application of a combined leaching protocol for the extraction of sedimentary Mn and Fe minerals revealed that mobilizable Mn(IV) represents the dominant Mn(oxyhydr)oxide phase with more than 70% of bulk solid-phase Mn. Steady state transport-reaction modeling showed that at postulated glacial O_2^{bw} of 35 μM, the oxic zone in the sediments was much more compressed than today where upward diffusing pore-water Mn^{2+} was oxidized and precipitated as authigenic Mn(IV) at the oxic-suboxic redox boundary in the upper 5 cm of the sediments. Transient transport-reaction modeling demonstrated that with increasing O_2^{bw} during the last glacial termination to current levels of $\sim$ 150 μM, (1) the oxic-suboxic redox boundary migrated deeper into the sediments and (2) the authigenic Mn(IV) peak was continuously mixed into subsequently deposited sediments by bioturbation causing the observed mobilizable Mn(IV) enrichment in the surface sediments. Such a distinct mobilizable Mn(IV) maximum was not found in the surface sediments of the APEI3 site, which indicates that the oxic zone was not as condensed during the LGP at this site due to two- to threefold lower organic carbon burial rates. Leaching data for sedimentary Fe minerals suggest that Fe(III) has not been diagenetically redistributed during the LGP at any of the investigated sites. Our results demonstrate that the basin-wide deoxygenation in the NE Pacific during the LGP was associated with (1) a much more compressed oxic zone at sites with carbon burial fluxes higher than 1.5 mg C_{org} m^{-2} d^{-1}, (2) the authigenic formation of a sub-surface mobilizable Mn(IV) maximum in the upper 5 cm of the sediments and (3) a possibly intensified suboxic-diagenetic growth of polymetallic nodules. As our study provides evidence that authigenic Mn(IV) precipitated in the surface sediments under postulated low glacial O_2^{bw}, it contributes to resolving a long-standing controversy concerning the origin of widely observed Mn-rich layers in glacial/deglacial deep-sea sediments.

1. Introduction

Some of the most extensive deposits of polymetallic nodules have been found in the Pacific Ocean, notably in the Clarion-Clipperton Zone (CCZ) in the NE Pacific (e.g., Halbach et al., 1988). Polymetallic nodules generally consist of irregular, concentrically

banded micro-layers of Mn and Fe (oxyhydr)oxides forming around a nucleus (e.g., Halbach et al., 1988). They precipitate either (1) hydrogenetically with dissolved or colloidal metals from seawater or (2) diagenetically by the supply of metals via the oxic-diagenetic (i.e. precipitation under oxic conditions) or suboxic-diagenetic (i.e. precipitation from suboxic pore water) growth pathways (e.g., Halbach et al., 1988). Hydrogenetic nodules are generally small ($\sim$ 1-5 cm) due to slow growth rates of about 1 to 10 mm Myr^{-1}, while diagenetic nodules are bigger (5 cm to more than 10 cm) as they grow at rates of several hundred millimeters per million years (e.g., Halbach et al., 1988). Most CCZ nodules show alternating Mn growth layers of hydrogenetic and diagenetic origin (e.g., Halbach et al., 1988; Wegorzewski and Kuhn, 2014; Heller et al., 2018). As the sediments of the CCZ are currently characterized by a broad upper oxic zone expanding over > 0.5 m, nodule growth is presently dominated by hydrogenetic and oxic-diagenetic accretion (e.g., Halbach et al., 1988; Mewes et al., 2014; 2016; Wegorzewski and Kuhn, 2014; Kuhn et al., 2017; Volz et al., 2018; Heller et al., 2018). The occurrence of older suboxic-diagenetic Mn growth layers indicates that suboxic surface sediment redox conditions may have occurred in the CCZ in the past (e.g., Wegorzewski and Kuhn, 2014; Heller et al., 2018). Further studies have shown that the upper 10-15 cm of the sediments of the eastern CCZ are characterized by solid-phase Mn enrichments (Mewes et al., 2014). Core-top solid-phase Mn peaks as well as Mn enrichments buried deeper in the sediments have also been observed in early studies from the eastern equatorial Pacific (Lynn and Bonatti, 1965; Berger et al., 1983; Finney et al., 1988; Piper, 1988), in the Atlantic Ocean (e.g., Froelich et al., 1979; Gingele and Kasten, 1994; Mangini et al., 2001) and more recently in the Southern Ocean (Presti et al., 2011; Jaccard et al., 2016; Wu et al., 2018). The formation of such sedimentary Mn maxima is controlled by primary input and diagenetic redistribution associated with the reductive dissolution of Mn (oxyhydr)oxides, during which Mn^{2+} diffuses upwards and re-precipitates as authigenic Mn(IV) during oxidation (e.g., Froelich et al., 1979; Burdige and Gieskes, 1983; Gingele and Kasten, 1994). However, the current sediment redox zonation in the eastern Pacific (Mewes et al., 2014; Volz et al., 2018) as well as in the Southern Ocean (e.g., Presti et al., 2011) does not allow for the authigenic formation of the observed MnO$_2$ enrichments at shallow sediment depth. Sediment leaching experiments for the extraction of the mobilizable Mn(IV) phase after Koschinsky et al. (2001) from Mn-rich CCZ surface sediments have revealed that the enrichment is dominated by mobilizable Mn(IV), which is reductively dissolved under slightly reducing conditions (Koschinsky et al., 2001; Mewes et al., 2014). Considering ^{10}Be/^{9}Be-based sedimentation rates of less than 0.6 cm kyr^{-1} (Mewes et al., 2014), this mobilizable Mn(IV) enrichment is associated with sediments deposited up to 30 kyr before present (BP). This includes sediment deposits of the last glacial maximum (LGM; $\sim$ 21 kyr BP), which are currently located at $\sim$ 10 cm depth. Thus, a more compressed oxic zone than currently observed may have allowed for Mn^{2+} to diffuse upwards and precipitate as an authigenic Mn(IV) phase close to the sediment surface during the last glacial period (LGP; $\sim$ 15-28 kyr BP) and may also have facilitated the suboxic-diagenetic accretion of polymetallic nodules (e.g., Wegorzewski and Kuhn, 2014).

Several studies have suggested that the widely observed solid-phase Mn maxima in deep-sea sediments throughout the global ocean are relics of the onset of ocean ventilation at glacial/interglacial transitions since middle Pleistocene ages when the bottom water was oxygenated (e.g., Mangini et al., 1990; 2001; Jaccard et al., 2009; 2016; Wu et al., 2018). More precisely, the authors proposed that less oxygenated bottom water during glacial periods may have facilitated pore-water Mn^{2+} diffusion from deeper sediments into surface sediments (e.g., Jaccard et al., 2009; 2016; Wu

et al., 2018), or even, into suboxic bottom waters (e.g., Mangini et al., 1990). At the last glacial termination (LGT) and, presumably, at each preceding glacial/interglacial transition, the onset of ocean ventilation oxygenated the bottom water and might have caused the oxidation of Mn^{2+} and subsequent burial of authigenic Mn (oxyhydr)oxides (e.g., Mangini et al., 1990; Wu et al., 2018). However, recent studies have provided compelling evidence that while bottom-water oxygen concentrations (O$_2^{bw}$) during the LGP were significantly lower throughout the eastern Pacific Ocean than today, they did not reach suboxic levels (Bradtmiller et al., 2010; Jacobel et al., 2017; Hoogakker et al., 2018; Anderson et al., 2019).

Other redox-sensitive elements such as U also indicate that the oxic-suboxic redox boundary was located at shallow sediment depths during the LGP as authigenic U(IV) enrichments are found in glacial deposits at various locations in the eastern Pacific (e.g., Bradtmiller et al., 2010; Jacobel et al., 2017). Authigenic U(IV) precipitates under similar reducing sediment redox conditions at which pore-water nitrate is consumed and the dissimilatory Fe(III) reduction commences (e.g., Froelich et al., 1979; Jacobel et al., 2017). Based on paleomagnetic sediment data of the abyssal NW Pacific, Korff et al. (2016) have identified magnetite-depleted glacial sediments, which were attributed to low O$_2^{bw}$ causing the reductive dissolution of magnetite.

Past changes in sediment redox conditions can be reconstructed based on the assemblage and reactivity of sedimentary Mn and Fe minerals, which can be determined by using sequential leaching protocols (e.g., Koschinsky et al., 2001; Poulton and Canfield, 2005). Here, we apply a combined leaching scheme based on the protocols by Koschinsky et al. (2001) and Poulton and Canfield (2005) for the organic-carbon-lean and mostly oxic sediments of the CCZ in order to determine different Mn and Fe pools, including (1) carbonate-associated Fe and Mn, (2) easily reducible Mn (oxyhydr)oxides, (3) easily reducible Fe oxides, (4) reducible Fe oxides and (5) magnetite. We have studied surface sediments from six sites located in European contract areas for the exploration of polymetallic nodules within the CCZ, and one site situated in an Area of Particular Environmental Interest (APEI3) north of the CCZ. We hypothesize that lower O$_2^{bw}$ during the LGP allowed upward diffusing Mn^{2+} to precipitate as authigenic Mn(IV) close to the sediment surface. Furthermore, we propose that the authigenic Mn(IV) peak was continuously mixed into subsequently deposited sediments due to bioturbation, which caused the observed Mn(IV) enrichments in the upper 10-15 cm of the CCZ sediments. We applied one-dimensional transport-reaction modeling to assess whether significantly lower glacial O$_2^{bw}$ could have created a much more compressed oxic zone than currently observed in CCZ sediments.

2. Material and methods

As part of the BMBF-EU JPI Oceans pilot action "Ecological Aspects of Deep-Sea Mining (MiningImpact)", multicorer (MUC) and 10-m-long gravity corer (GC) sediment cores were collected during RV SONNE cruise SO239 in 2015 (Martínez Arbizu and Haeckel, 2015). The MUC sediment cores were retrieved from four European contract areas for the exploration of polymetallic nodules and from one of the Areas of Particular Environmental Interest (APEI3) (Fig. 1; Table 1). The investigated contract areas include the German BGR (Bundesanstalt für Geowissenschaften und Rohstoffe) area, the Belgian GSR (Global Sea Mineral Resources NV) area, the French IFREMER (Institut Français de Recherche pour l'Exploitation de la Mer) area and the Eastern European IOM (InterOceanMetal) area, while the APEI3 is excluded from any potential mining activities. Two sites are located in the BGR area, namely in the "reference area" (BGR-RA) and in the "prospective area" (BGR-PA) for potential future polymetallic nodule exploitation. For the de-

Table 1

Investigated MUC sampling sites with geographic position and water depth. If not indicated otherwise, sampling station characteristics, such as sedimentation rate (Sed. rate), flux of particulate organic carbon (POC) to the seafloor, bioturbation depth (Bioturb. depth), oxygen penetration depth (OPD) and nodule size are taken from Volz et al. (2018). Information for site SO205-65 is taken from Rühlemann et al. (2010) and Mewes et al. (2016). For the BGR-PA site, information is taken from an adjacent site (A5-2-SN; 11°57.22′N, 117°0.42′W) studied by Mewes et al. (2014) and Mogollón et al. (2016). Note that the threefold higher POC flux for the BGR-PA site compared to the other sites is highly unlikely and probably an artifact derived from the choice of the organic matter degradation coefficient in the transport-reaction model by Mogollón et al. (2016).

| Site	Latitude (N)	Longitude (W)	Water depth (m)	Sed. rate (cm kyr^{-1})	POC flux (mg C$_{org}$ m^{-2} d^{-1})	Bioturb. depth (cm)	OPD (m)	Nodule size
SO205-65	13°10.50′	118°06.30′	4283.0	0.38[a]	1.2[a]	5[a]	oxic[a]	small to medium[b]
BGR-PA	11°50.64′	117°03.44′	4132.0	~0.53[c]	~6.9[c]	~5[c]	~2[c,d]	medium[e]
BGR-RA	11°49.13′	117°33.13′	4314.8	0.65	1.99	7	0.5	medium
IOM	11°04.73′	119°39.48′	4430.8	1.15	1.54	13	3	medium
GSR	13°51.25′	123°15.30′	4517.7	0.21	1.51	8	>7.4	big
IFRE-1	14°02.62′	130°08.32′	4918.8	0.64	1.47	7	4.5	medium
IFRE-2	14°02.45′	130°05.11′	5005.5	0.48	1.5	8	3.8	no nodules
APEI3	18°47.46′	128°22.42′	4816.6	0.2	1.07	6	>5.7	small

[a] Mewes et al. (2016).
[b] Rühlemann et al. (2010).
[c] Mogollón et al. (2016).
[d] Mewes et al. (2014).
[e] Martínez Arbizu and Haeckel (2015).
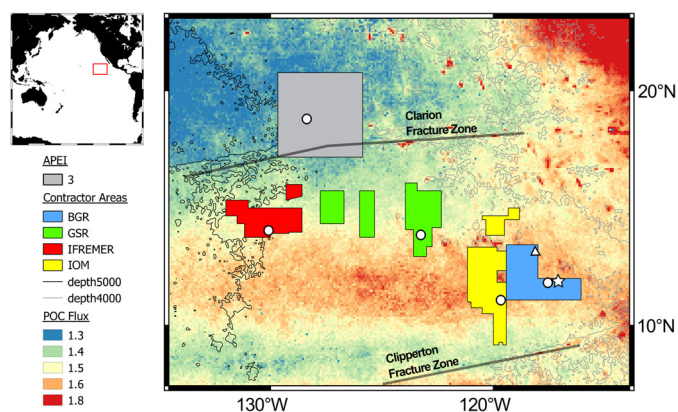
Fig. 1. Map of the investigated sampling sites (open circles, star and triangle) in the different European contract areas for the exploration of polymetallic nodules and in the APEI3. The IFRE-1 and IFRE-2 sites are both located in the IFREMER area (open circle). The BGR area includes the BGR-RA (open circle), BGR-PA (open star) and SO205-65 (open triangle; Rühlemann et al., 2010; Mewes et al., 2016) sites. Background colors indicate the maximum POC flux [mg C$_{org}$ m^{-2} d^{-1}] to the seafloor estimated by Lutz et al. (2007). Map is modified after Volz et al. (2018).

velopment of the combined leaching procedure, we used sediment samples of MUC core SO205-65 retrieved from the BGR area during RV SONNE cruise SO205 in 2010 in the framework of the MAN-GAN project (Fig. 1; Table 1; Rühlemann et al., 2010; Mewes et al., 2016).

The surface sediments throughout the investigated contract areas are characterized by clay-dominated siliceous oozes with variable nodule sizes (1-10 cm) and distributions at the seafloor (Table 1; Mewes et al., 2014; Volz et al., 2018). All MUC sediment cores investigated in this study are oxic throughout (Volz et al., 2018). In order to characterize the investigated sites, key parameters, including sedimentation rate, depositional flux of particulate organic carbon (POC), bioturbation depth and oxygen penetration depth (OPD) are summarized in Table 1, which were originally presented elsewhere and are based on studies of 10 to 14-m-long GC and piston cores (Mewes et al., 2014, 2016; Mogollón et al., 2016; Volz et al., 2018). At most of the investigated sites, suboxic conditions are found at different depth below the OPD, where the reduction of Mn(IV) and nitrate coexist in the absence of oxygen and sulfide. Dissolved Fe^{2+} was not detected at any of the sites (Mogollón et al., 2016; Volz et al., 2018).

2.1. Sediment sampling

Immediately after core recovery, all MUC sediment cores were transferred into the cold room at a temperature of ~ 4 °C. Sediment sampling was performed in 1 cm resolution and every 2 cm at the IOM site. All sediment samples were taken with a plastic spatula and stored in plastic vials at −20 °C until further analysis.

2.2. Total acid digestion

Total acid digestions were performed in a microwave system MARS Xpress (CEM) with the evaporation accessory CEM Xpress-Vap. About 50 mg of freeze-dried, homogenized bulk sediment were digested in an acid mixture of 65% sub-boiling distilled HNO$_3$ (3 mL), 30% sub-boiling distilled HCl (2 mL) and 40% suprapur® HF (0.5 mL) at ~ 230 °C. Bulk Mn, Fe and Al contents were determined using inductively coupled plasma optical emission spectrometry (IRIS Intrepid ICP-OES Spectrometer, Thermo Elemental). Based on the standard reference material NIST 2702 accuracy and precision of the analysis was 5.9% and 3.7% for Al, 7.1% and 4.6% for Fe and 3.7% and 3.5% for Mn, respectively ($n = 67$). Bulk sediment data have been corrected post-analytically for the interference of the pore-water salt matrix on the sediment composition (Volz et al., 2018). Bulk Mn and Fe contents were normalized to Al in order to calculate the excess fractions relative to the pelagic background sedimentation.

2.3. Sequential extraction of Mn and Fe (oxyhydr)oxides

A specific extraction protocol for the separation of Mn and Fe (oxyhydr)oxides from Pacific sediments and Mn nodules has been presented by Koschinsky et al. (2001). Poulton and Canfield (2005) have developed a sequential leaching procedure, which targets different sedimentary Fe pools. In order to determine the availability and reactivity of both Mn and Fe mineral phases, and to reconstruct the potential past redox cycling of Mn and Fe, we have combined these two procedures.

2.3.1. Combined leaching protocol: method testing

The protocols by Koschinsky et al. (2001) and Poulton and Canfield (2005) have first been separately applied on sediments of core SO205-65 (Table 1) to test their selectivity for Mn (oxyhydr)oxides and various Fe minerals (Fig. 2). About 100 mg of freeze-dried homogenized sediment were sequentially treated with 10 mL of the
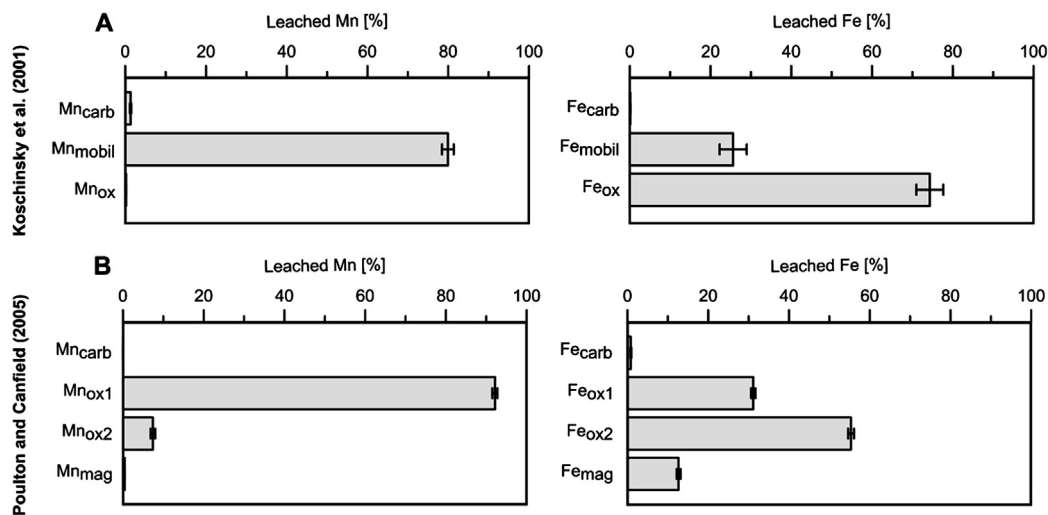
Fig. 2. Method test of the leaching protocols after (A) Koschinsky et al. (2001) and (B) Poulton and Canfield (2005) separately applied on sediment samples from MUC core SO205-65 (Fig. 1; Table 1). Sequentially leached percentages of Mn and Fe oxides after the protocol by Koschinsky et al. (2001) (Mn_{carb}, Fe_{carb}; Mn_{mobil}, Fe_{mobil}; Mn_{ox}, Fe_{ox}) and Poulton and Canfield (2005) (Mn_{carb}, Fe_{carb}; Mn_{ox1}, Fe_{ox1}; Mn_{ox2}, Fe_{ox2}; Mn_{mag}, Fe_{mag}) are shown with respect to bulk sediment contents of Mn and Fe (Mn_{total}; Fe_{total}). For the respective extraction reagents used during each leaching step see Table 2. Note that Mn_{ox}, Fe_{ox} after the protocol of Koschinsky et al. (2001) is extracted with 0.2 M ammonium oxalate/0.2 M oxalic acid.

Table 2
Protocol for the combined leaching scheme combining the methods after Koschinsky et al. (2001) and Poulton and Canfield (2005).

Step	Associated mineral phase	Terminology	Extraction reagent[a]	Extraction time	pH
I	Carbonate-associated Fe and Mn	Mn_{carb} Fe_{carb}	1 M Na-acetate	24 h	4.5
II	Mobilizable Mn and associated Fe	Mn_{mobil} Fe_{mobil}	0.1 M hydroxylamine-HCl	2 h	2
III	Easily reducible Fe oxides and associated Mn	Fe_{ox1} Mn_{ox1}	1 M hydroxylamine-HCl	48 h	
IV	Reducible Fe oxides	Fe_{ox2}	Na-dithionite (50 g L^{-1})/0.2 M Na-citrate solution	2 h	4.8
V	Magnetite	Fe_{mag}	0.2 M ammonium oxalate/0.17 M oxalic acid	6 h	

[a] All extraction steps performed at $\sim 20\,^\circ$C.

respective extraction reagents for given reaction times (Koschinsky et al., 2001; Poulton and Canfield, 2005) and centrifuged afterwards (4000 rpm, 5 min). The supernatant extraction solutions were filtered through a 0.2 μm polyethersulfone membrane before Mn and Fe concentrations were determined upon dilution using ICP-OES (IRIS Intrepid ICP-OES Spectrometer, Thermo Elemental). Calibration standards were produced in 0.3 M HNO_3 or in Milli-Q® (Na-dithionite; see Table 2) and adjusted to the different reagent matrices in order to prevent matrix effects during analysis.

The first two leaching steps primarily mobilize adsorbed and pore-water cations as well as carbonate-associated Fe and Mn, respectively (Koschinsky et al., 2001; Poulton and Canfield, 2005). As the concentrations of Fe and Mn were below detection limit during the method test with SO205-65 sediment samples (Fig. 2), the first two steps were merged in the combined extraction protocol (Table 2, step I). The major difference between the both extraction protocols is the concentration, pH value and reaction time of the extraction reagent hydroxylamine-HCl. As Koschinsky et al. (2001) have intended to only extract the easily mobilizable Mn fraction, the 0.1 M hydroxylamine-HCl solution is adjusted to pH 2, while Poulton and Canfield (2005) have used a 1 M hydroxylamine-HCl in 25% v/v acetic acid solution for the extraction of easily reducible Fe oxides at pH < 2. On average, 74% of bulk sediment Mn (Mn_{total}) is extracted with 0.1 M hydroxylamine-HCl (Mn_{mobil}) (Fig. 2A). In order to separate mobilizable Mn (oxyhydr)oxides (Mn_{mobil}) from easily reducible Fe (oxyhydr)oxides (Fe_{ox1}) in the combined extraction protocol, the sediment samples are sequentially treated with 0.1 M hydroxylamine-HCl and

1 M hydroxylamine-HCl (Table 2, step II and III, respectively). Only 2% of bulk sediment Fe (Fe_{total}) are mobilized with 0.1 M hydroxylamine-HCl (Fe_{mobil}) representing easily reducible Fe (oxyhydr)oxides (Fig. 2A). The remaining fraction of easily reducible Fe (oxyhydr)oxides is extracted with 1 M hydroxylamine-HCl (Table 2). Using the protocol after Poulton and Canfield (2005), an average of 20% of Fe_{total} is extracted by Na-dithionite (Fe_{ox2}) and 5% by ammonium oxalate (Fe_{mag}; Fig. 2B). Therefore, we have implemented these extraction steps into the combined leaching protocol (Table 2, step IV and V, respectively).

2.3.2. Application of the combined leaching protocol

For the sequential extraction of Mn and Fe (oxyhydr)oxides of sediment samples from RV SONNE cruise SO239 investigated in this study, the combined leaching procedure was performed on samples taken every 3 cm using acid-cleaned vials (Table 2). Since the process of freeze-drying might increase the crystallinity of Mn and Fe (oxyhydr)oxides (e.g., Rapin et al., 1986), fresh sediment samples equivalent to $\sim$ 100 mg of dry sediment were used. Dry sediment masses were calculated using the mass of the interstitial water (Volz et al., 2018). In order to monitor the recovery of the sequential extractions, the sediment residues were completely dissolved after the last extraction step (see section 2.1). The recovery is defined as the sum of leachable contents (step I-V, Table 2) and residual contents divided by bulk contents. It was determined for three sediment cores with systematically high values for Fe (104-124%) and Mn (96-143%). These elevated recoveries are most likely caused by the slight sediment inhomogeneity of fresh sedi-
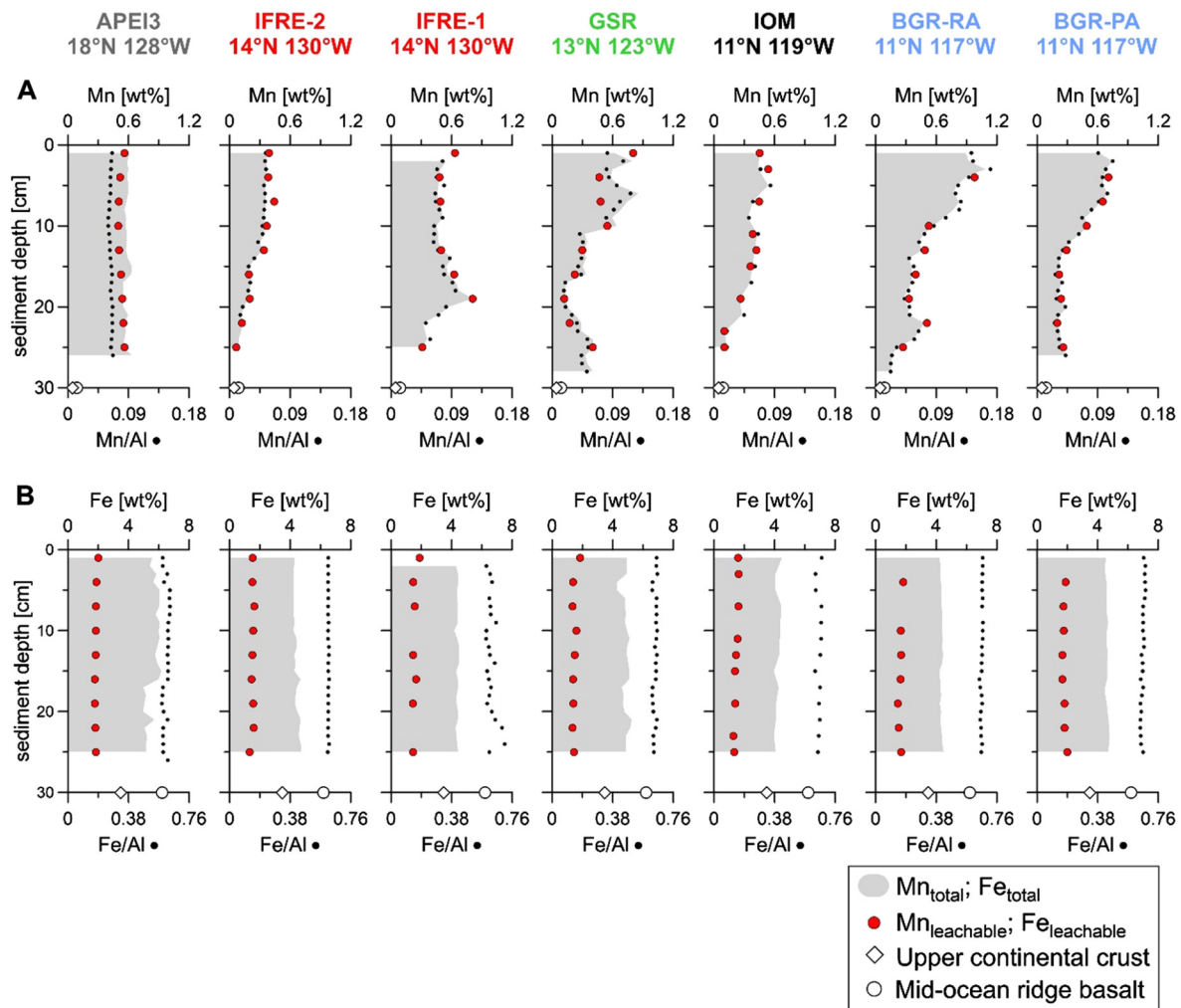
Fig. 3. Bulk sediment contents of Mn and Fe (Mn_{total}; Fe_{total}), total leachable contents of Mn and Fe ($Mn_{leachable}$; $Fe_{leachable}$) using the combined leaching protocol (Table 2) and Mn_{total}/Al_{total} and Fe_{total}/Al_{total} ratios (black dots) for all investigated sites. Average ratios of Mn/Al and Fe/Al for the upper continental crust (diamond) and mid-ocean ridge basalts (circle) are taken from Rudnick and Gao (2004) and Klein (2004), respectively.

ment samples used for the combined leaching protocol, while bulk contents were determined on freeze-dried, homogenized samples. Furthermore, as we have not washed the sediment samples in between the extraction steps, higher recovery values for the leached sediments could also be associated with a successive carry-over of Mn and Fe due to the incomplete removal of the extraction reagent after the respective leaching step. The %RSD was determined based on triplicate measurement of each sample and was < 2% for Mn and < 2.8% for Fe. Based on in-house reference material, the analytical precision was < 6% for Fe and Mn ($n = 12$).

### 2.4. Geochemical model setup and reaction network

A one-dimensional steady state transport-reaction model, which couples biogeochemical reactions through a discretized steady state transport-reaction equation (e.g., Boudreau, 1997) was used to assess whether postulated glacial O_2^{bw} of 35 μM (Hoogakker et al., 2018; Anderson et al., 2019) could have caused a near-surface oxic-suboxic redox boundary. We have applied the model for the BGR-RA, IFRE-2 and APEI3 sites in order to cover a large area in the CCZ over a distance of about 1300 km (Fig. 1). The simulations were performed for the upper 2 m at the BGR-RA site, 7.5 m at the IFRE-2 site and 6 m at the APEI3 site using pore-water data from 10-m-long GC cores published in Volz et al. (2018) (Supplementary Table S1). Additionally, a transient transport-reaction

model (Eq. S1; S2) was applied in order to simulate the depth distribution of mobilized Mn(IV) contents for the last 21 kyr. For this simulation, we have assumed that O_2^{bw} of 35 μM have prevailed between 15-21 kyr BP (Hoogakker et al., 2018; Anderson et al., 2019). Between 14-15 kyr BP, O_2^{bw} is assumed to have increased linearly to current concentrations of 120 μM, 150 μM and 160 μM, respectively (Volz et al., 2018; Hoogakker et al., 2018). A detailed description of the model setup, parameterization and sensitivity tests is presented in the Supplementary material S1. All species, parameters, boundary conditions and reaction terms are listed in the Supplementary Tables S1 and S2.

3. Results

3.1. Bulk sediment

Total solid-phase Mn contents (Mn_{total}) in the upper 25 cm of the sediments are within 0.1 and 1 wt% at all sites (Fig. 3A) with downward decreasing contents at both BGR sites, the GSR and the IFRE-2 sites. At the IFRE-1 site, Mn_{total} does not decrease with depth but shows a subsurface peak of 0.8 wt% at 20 cm depth. In contrast to overall downward decreasing solid-phase Mn contents at most sites, Mn_{total} contents remain relatively constant in the sediments at the APEI3 site at 0.6 wt% throughout the sediment core. The profiles of bulk sediment Mn/Al mimic the Mn_{total} profiles at all sites and range between 0.01 and 0.17 (Fig. 3A).
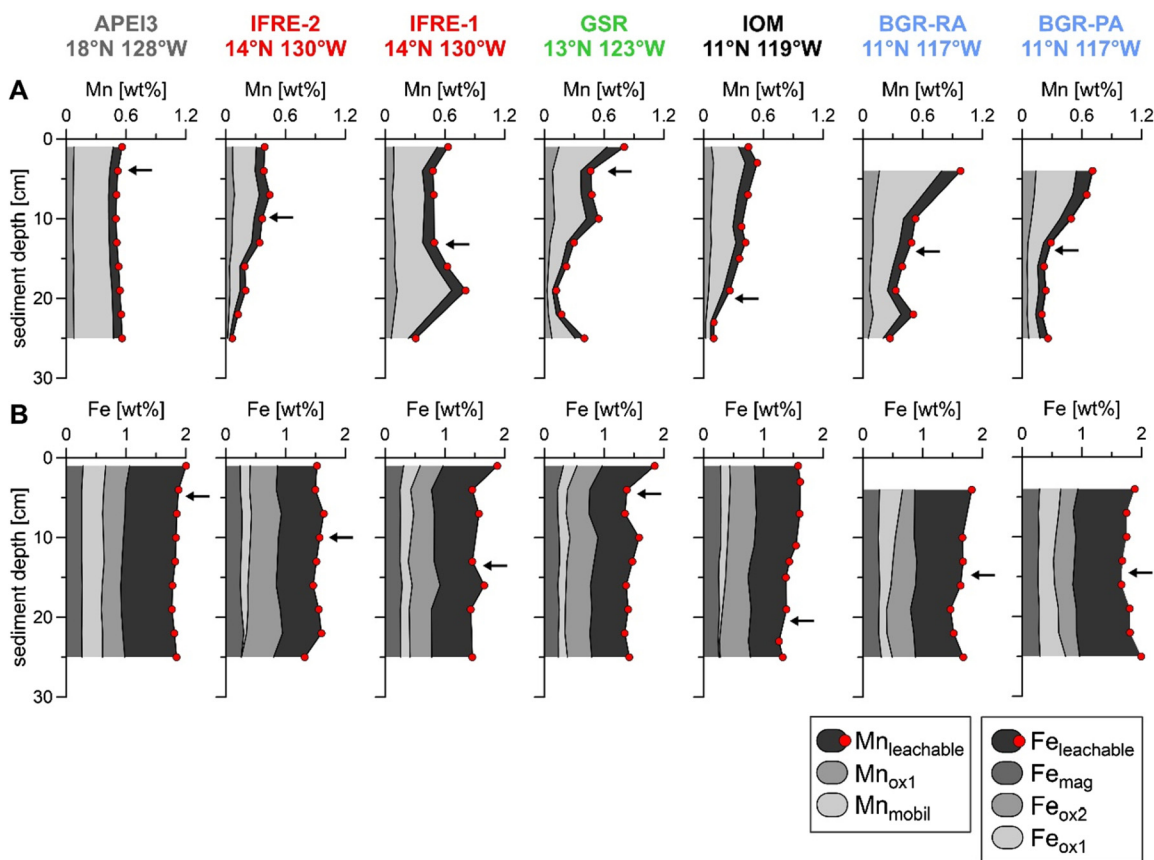
Fig. 4. Total leachable contents of Mn and Fe (Mn$_{leachable}$; Fe$_{leachable}$) and contents of sequentially leached Mn oxides (Mn$_{mobil}$, Mn$_{ox1}$) and Fe oxides (Fe$_{ox1}$ (including Fe$_{mobil}$); Fe$_{ox2}$; Fe$_{mag}$) using the combined leaching protocol (Table 2) for all investigated sites. Black arrows indicate the location of the LGM sediment surface based on ^{230}Th/^{231}Pa-derived sedimentation rates (Table 1).

Total Fe contents (Fe$_{total}$) vary between 4 and 5 wt% at all sites except for the APEI3 site, where Fe$_{total}$ is between 5 and 6 wt% (Fig. 3B). Bulk sediment Fe/Al profiles resemble the Fe$_{total}$ profiles at all sites within the range of 0.6 and 0.7 (Fig. 3B).

3.2. Leachable Mn and Fe (oxyhydr)oxides

In total, more than 85% of Mn$_{total}$ is extracted (Mn$_{leachable}$) during the combined sequential leaching procedure (Fig. 3A). Only 30-40% of Fe$_{total}$ is leached with the combined extraction scheme (Fe$_{leachable}$; Fig. 3B). The depth profiles of Mn$_{leachable}$ and Fe$_{leachable}$ mimic the bulk contents Mn$_{total}$ and Fe$_{total}$, respectively, at all sites.

Between 94 and 99% of Mn$_{leachable}$ is leached in the Mn$_{mobil}$ and Mn$_{ox1}$ fractions at all sites (Table 2; Fig. 4A). Mn$_{mobil}$ contents fluctuate between 0.1 and 0.8 wt%, while Mn$_{ox1}$ contents are below 0.2 wt% (Fig. 4A). Between 92 and 96% of Fe$_{leachable}$ is leached in the Fe$_{ox1}$ (including Fe$_{mobil}$), Fe$_{ox2}$ and Fe$_{mag}$ fractions with contents of 0.25-0.65 wt%, 0.75-1 wt% and 0.22-0.32 wt%, respectively (Table 2; Fig. 4B).
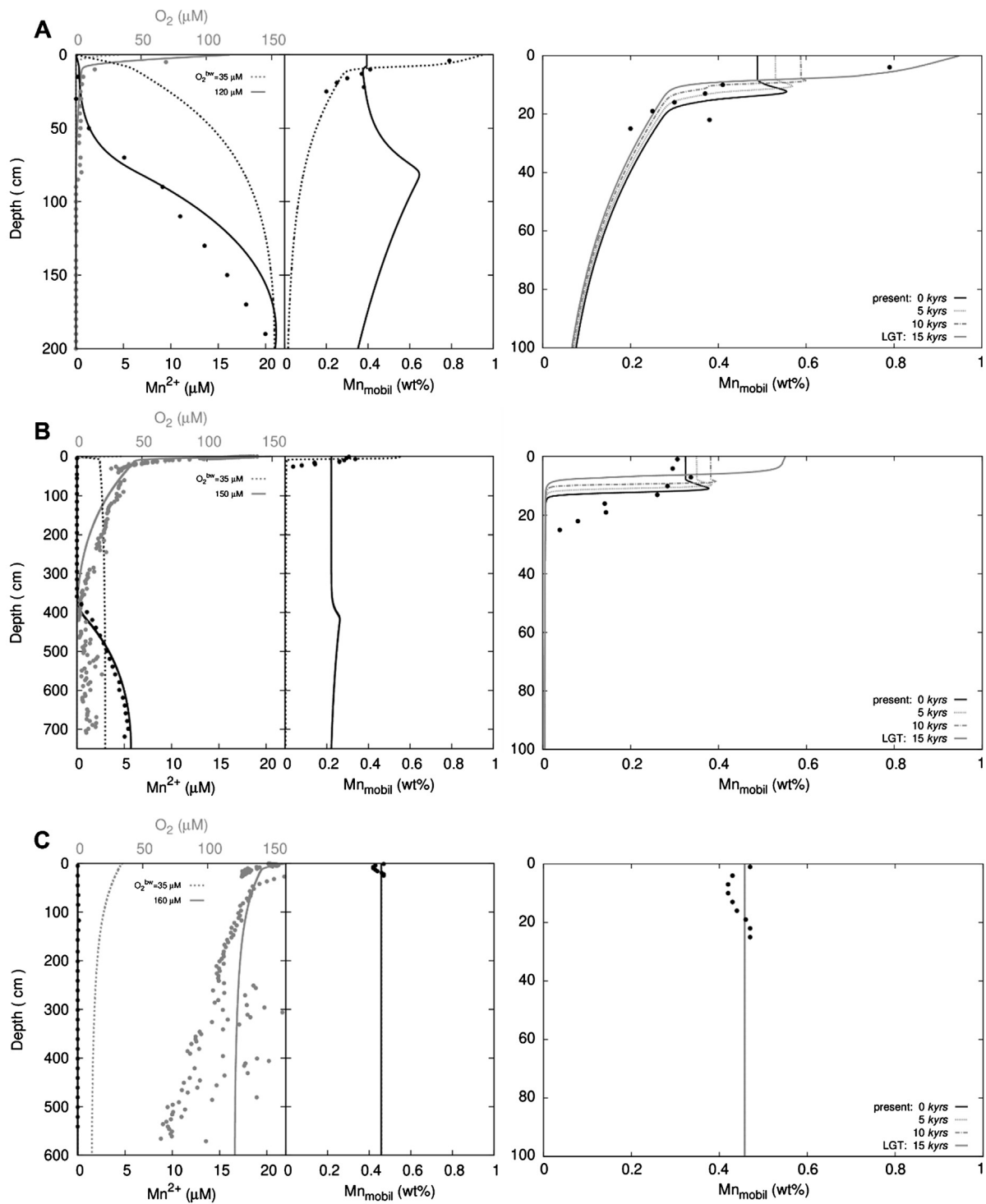
3.3. Transport-reaction modeling

Transport-reaction simulations were performed for the BGR-RA, IFRE-2 and APEI3 sites (Fig. 5). At current O$_2^{bw}$ of 120 μM at the BGR-RA site, 150 μM at the IFRE-2 site, authigenic Mn(IV) (Mn$_{mobil}$) precipitates at the current oxic-suboxic redox boundary at 0.5 m and 3.8 m depth, respectively (Table 1; Volz et al., 2018). At current O$_2^{bw}$ of 160 μM at the APEI3 site, oxygen penetrates at least 5.7 m into the sediments, and thus, authigenic Mn$_{mobil}$ is currently not forming in the recovered sediments (Table 1; Volz et al., 2018). At postulated glacial O$_2^{bw}$ of 35 μM, the oxic-suboxic re-

dox boundary is located at 5 cm depth at the BGR-RA and IFRE-2 sites. Consequently, high Mn$_{mobil}$ contents of 0.95 wt% and 0.55 wt% form in the upper 5 cm of the sediments at the BGR-RA and IFRE-2 sites, respectively (Fig. 5A and 5B). Below, Mn$_{mobil}$ contents decrease sharply with depth with a residual Mn$_{mobil}$ fraction below the oxic-suboxic redox boundary at the BGR-RA site. At the APEI3 site, postulated glacial O$_2^{bw}$ of 35 μM induce overall lower oxygen concentrations in the sediments but suboxic conditions are not reached (Fig. 5C). Therefore, the Mn$_{mobil}$ fraction shows constant contents of 0.45 wt% over depth at the APEI3 site resulting from the initial depositional flux of Mn (see Supplementary Tables S1). The transient transport-reaction model reveals that after the increase of O$_2^{bw}$ from 35 μM to current oxygen levels between 14-15 kyr BP, Mn$_{mobil}$ contents are mostly steady throughout the upper 7 cm of the sediments with Mn$_{mobil}$ contents of almost 0.6 wt% and 0.4 wt% at the BGR-RA and IFRE-2 sites, respectively (Fig. 5). At present, Mn$_{mobil}$ contents are 0.5 wt% and 0.3 wt% at the BGR-RA and IFRE-2 sites, respectively. Below a subsurface Mn$_{mobil}$ peak at 15 cm depth, Mn$_{mobil}$ contents decrease sharply with depth at the BGR-RA and IFRE-2 sites. The transient transport-reaction model for the APEI3 site shows that the depth distribution of Mn$_{mobil}$ remains constant over time (Fig. 5C).

4. Discussion

4.1. Past redox changes in sediments of the CCZ

Highest bulk Mn contents (Mn$_{total}$) of up to 1 wt% occur in the upper 10 cm of the oxic sediments at most of the sites with bulk Mn/Al values well above the average ratios of the upper continental crust and mid-ocean ridge basalts (Fig. 3A; Rudnick and

Fig. 5. Model results for the BGR-RA site (A), the IFRE-2 site (B) and the APEI3 site (C) including the steady state transport-reaction simulations (left) and the transient transport-reaction simulations (right). Concentrations of oxygen (grey dots) and Mn^{2+} (black dots) for 10-m-long GC cores were taken from Volz et al. (2018). Left: Simulations were performed for current bottom-water oxygen concentrations (O_2^{bw}) of 120 μM for the BGR-RA site (solid line), 150 μM for the IFRE-2 site (solid line), 160 μM for the APEI3 site (solid line) and glacial O_2^{bw} of 35 μM (dashed line). The depth distribution of Mn_{mobil} is simulated for every site for the respective current O_2^{bw} between 120 μM and 160 μM (solid line) and glacial O_2^{bw} of 35 μM (dashed line) using the steady state model. Right: Transient simulations for the depth distribution of Mn_{mobil} in the upper 100 cm of the sediments after linearly increasing O_2^{bw} from 35 μM to 120 μM (BGR-RA), 150 μM (IFRE-2) and 160 μM (APEI3) between 14-15 kyr. Measured contents of mobilizable Mn(IV) (Mn_{mobil}) are indicated (black dots).

Gao, 2004; Klein, 2004). Similar bulk Mn distribution patterns have been reported for other sites within the CCZ (e.g., Finney et al., 1988; Piper, 1988; Mewes et al., 2014; Heller et al., 2018). The modern geochemical zonation in CCZ sediments does not allow for upward diffusing Mn^{2+} to precipitate as authigenic Mn(IV)

at a depth shallower than the current OPD below 0.5 m depth (Table 1; Fig. 5; Mewes et al., 2014; 2016; Kuhn et al., 2017; Volz et al., 2018). Therefore, we suggest that the near-surface Mn_{total} maxima (Fig. 3A) has formed under conditions, when the oxic-suboxic redox boundary was located at shallower depth in the

past. This assumption is supported by the applied combined leaching procedure to determine the mobilizable Mn contents (Mn_{mobil}), which represents > 70% of Mn_{total} (Fig. 4A). The Mn_{mobil} fraction has most likely been diagenetically redistributed in the past under suboxic conditions and precipitated as authigenic Mn_{mobil} phase at a shallow oxic-suboxic boundary (e.g., Koschinsky et al., 2001; Mewes et al., 2014). Further indication for past near-surface suboxic conditions in CCZ sediments is provided by surface nodules and buried nodules, which consist of alternating hydrogenetic and suboxic-diagenetic Mn layers (e.g., Halbach et al., 1988; Wegorzewski and Kuhn, 2014; Heller et al., 2018). While hydrogenetic and oxic-diagenetic accretion currently dominates nodule growth, older suboxic-diagenetic Mn growth layers found in nodules of the BGR area provide evidence for a more condensed oxic zone in the past (e.g., Wegorzewski and Kuhn, 2014). In addition, partially dissolved Mn layers found in buried nodules in oxic sediments strongly suggest that the OPD must have been located at shallower depth in the past (Heller et al., 2018). The $^{230}Th/^{231}Pa$-based sedimentation rates at the investigated sites determined by Volz et al. (2018) range between 0.2-1.2 cm kyr^{-1} (Table 1), and thus, sediments containing the authigenic Mn_{mobil} enrichment were usually deposited within the last 20-30 kyr, including deposits from the LGM (Fig. 4A).

The observed Mn_{mobil} enrichments in the uppermost 10 cm of the sediments at most of the investigated sites in the CCZ indicate that diagenetic redistribution of Mn has occurred widespread throughout the NE Pacific (Figs. 3 and 4; Mewes et al., 2014). In contrast, constant Mn_{mobil} contents throughout the upper 25 cm at the APEI3 site suggest that Mn(IV) has not been diagenetically mobilized at this site in the past (Figs. 3 and 4). The depth position of the sedimentary oxic-suboxic boundary is controlled by the burial flux of POC, O_2^{bw}, availability of Mn (oxyhydr)oxides and sedimentation rate (e.g., Froelich et al., 1979; Burdige and Gieskes, 1983; Gingele and Kasten, 1994). Compared to the other study sites, the POC flux to the seafloor at the APEI3 site is almost twofold lower (e.g., Lutz et al., 2007; Volz et al., 2018). Therefore, the sediments at the APEI3 site are currently dominated by an extensive oxic zone, penetrating more than 5.7 m into the sediment (Table 1). At this location, low POC fluxes to the seafloor of 1 mg C_{org} m^{-2} d^{-1} in combination with low sedimentation rates of 0.2 cm kyr^{-1} result in TOC burial rates that are two- to threefold lower than at the other study sites (Table 1; Volz et al., 2018). Due to these significantly lower carbon burial rates, the sediments at the APEI3 site have most likely never reached suboxic conditions in the past, and thus, did not experience significant suboxic-diagenetic Mn mobilization (Figs. 3A and 5C). This assumption is consistent with nodules at the sediment surface of APEI3 site, which are significantly smaller than at the sites within the exploration areas (Table 1). These small nodules most likely formed exclusively by hydrogenetic and oxic-diagenetic accretion and not via an alternation of hydrogenetic and suboxic-diagenetic accumulation as observed at the other CCZ study sites (Halbach et al., 1988; Wegorzewski and Kuhn, 2014; Heller et al., 2018). These findings are in agreement with a study on nodules and surface sediments from the adjacent APEI6 area, where nodules were shown to have formed exclusively by hydrogenetic and oxic-diagenetic growth (Menendez et al., 2018). Almost constant Mn_{mobil} contents in the surface sediments of the APEI6 area further indicate that Mn has not been subject to suboxic mobilization (Menendez et al., 2018). Accordingly, solid-phase Mn contents in the sediments at the APEI3 site are assumed to be exclusively of hydrogenetic origin. As the $^{230}Th/^{231}Pa$-based age record for the APEI3 site indicates relatively steady sedimentation rates over the past 125.000 years (Volz et al., 2018), we suggest that hydrogenetic Mn has been uniformly deposited over time from the water column to the CCZ seabed. As the APEI3 site shows the overall

lowest sedimentation rates of 0.2 cm kyr^{-1}, dilution of hydrogenetic Mn with other sediment components (terrigenous particles) is lower compared to the other study sites, and thus, Mn contents are similar.

In order to allow for the diagenetic redistribution of Mn in the sediments at most of the CCZ study sites, several factors have been reported to potentially cause a more condensed oxic zone than currently observed: (1) higher burial fluxes of particulate organic carbon (POC) to the seafloor due to higher surface water productivity, (2) lower O_2^{bw} inducing better preservation of organic matter or (3) a combination of both factors (e.g., Mewes et al., 2014; Wegorzewski and Kuhn, 2014; Heller et al., 2018). Compared to the CCZ, sediments of the manganese nodule field in the Peru Basin (PB) are currently characterized by much shallower OPDs of 5-15 cm depth (e.g., Haeckel et al., 2001). About twofold higher POC fluxes to the seafloor in the PB compared to the CCZ cause this condensed oxic zone, which allows suboxic-diagenetic accretion to contribute to nodule growth in the PB (e.g., Haeckel et al., 2001; Koschinsky et al., 2001). Thus, in order to have exceeded the flux of oxygen into the sediments and consequently compress the oxic zone in the sediments of the CCZ during the LGP, the POC flux to the seafloor must have been at least twofold higher than today (e.g., Wegorzewski and Kuhn, 2014). Studies have proposed that surface water productivity and POC burial in the eastern Pacific might have been increased during the LGP due to intensified trade winds and therefore enhanced nutrient upwelling and aeolian dust input (e.g., Thomas et al., 2000), which could have affected the CCZ sediments. However, a variety of complementary approaches has indicated that ocean dynamics, i.e. upwelling and stratification, impose a strong regulative effect on surface water productivity and the POC export to the deep ocean (e.g., Perks et al., 2002; Winckler et al., 2016; Costa et al., 2017). Studies using biogenic opal, Ba_{xs} and dust fluxes in the equatorial Pacific as well as selectively preserved organic matter compounds in the sediments have shown that higher POC fluxes have occurred after the LGP, namely during the last deglaciation (e.g., Bradtmiller et al., 2006; Anderson et al., 2019). Additionally, there is strong indication that lower O_2^{bw} have prevailed in the eastern Pacific during the LGP due to changes in ocean circulation rather than enhanced POC burial (e.g., Perks et al., 2002; Winckler et al., 2016; Costa et al., 2017). Throughout the eastern Pacific Ocean, independent proxies have provided evidence for lower O_2^{bw} during the LGP, including (1) sub-surface solid-phase Mn enrichments (Mangini et al., 1990), (2) the enrichment of authigenic U(IV) in LGP deposits (e.g., Jaccard et al., 2009; Bradtmiller et al., 2010; Jacobel et al., 2017), (3) the carbon isotope composition and I/Ca ratios in planktonic foraminifera (e.g., Hoogakker et al., 2018) and (4) geochemical proxies for the differences in POC rain rate and the preservation of organic compounds (Anderson et al., 2019). Although the glacial bottom water was not suboxic, which has been suggested by Mangini et al. (1990), oxygen was probably mostly consumed in the sediments as a result of significantly lower O_2^{bw} than today (Jaccard et al., 2009; Hoogakker et al., 2018; Anderson et al., 2019).

4.2. Diagenetic Mn mobilization during the last glacial period

In order to assess whether lower glacial O_2^{bw} may have facilitated the development of a shallow oxic-suboxic redox boundary, we have performed steady state transport-reaction modeling for the BGR-RA, IFRE-2 and APEI3 sites (Fig. 5). Furthermore, we used a transient model to simulate the authigenic Mn_{mobil} depth distribution during the downward migration of the oxic-suboxic boundary at the last glacial termination (LGT; Fig. 5; e.g., Hoogakker et al., 2018). Hoogakker et al. (2018) and Anderson et al. (2019) have reconstructed low O_2^{bw} for the LGM in the eastern equatorial Pacific within the range of 35-55 μM, which we have

Table 3

Model-derived downward O_2 fluxes and upward Mn^{2+} fluxes at the sediment-water interface (SWI) for glacial bottom-water oxygen concentrations (O_2^{bw}) of 35 µM (e.g., Hoogakker et al., 2018; Anderson et al., 2019) and current O_2^{bw} of 120 µM at the BGR-RA site, 150 µM at the IFRE-2 site and 160 µM at the APEI3 site (Volz et al., 2018) and recycling of 60% of the upward diffusing Mn^{2+} by hydrogenetic re-precipitation in the water column using the recycling coefficient ε_{Mn} after Katsev et al. (2007).

Site	O_2^{bw}	O_2 flux at SWI (µmol O_2 cm^{-2} yr^{-1})	Mn^{2+} flux at SWI (µmol Mn cm^{-2} yr^{-1})	Mn^{2+} recycling (ε_{Mn}) at SWI (µmol Mn cm^{-2} yr^{-1})
BGR-RA	35 µM	5.976	−0.052	0.0312
BGR-RA	120 µM	6.009	−0.003	0.0018
IFRE-2	35 µM	4.215	−0.037	0.0222
IFRE-2	150 µM	4.537	−6E-5	3.6E-5
APEI3	35 µM	0.327	−6E-6	3.6E-6
APEI3	160 µM	0.324	−1E-7	6E-8

applied for the glacial scenario in the transport-reaction model (Supplementary Table S1). For the transient approach, we assumed that O_2^{bw} increased between 14-15 kyr from 35 µM to current oxygen levels of 120 µM at the BGR-RA site, 150 µM at the IFRE-2 site, and 160 µM at the APEI3 site (Volz et al., 2018; Hoogakker et al., 2018). The initial depositional flux of Mn (oxyhydr)oxides was assumed to be independent of O_2^{bw} and has been estimated based on the terrigenous-free bulk Mn accumulation rate at the APEI3 site, where Mn(IV) most probably has not been diagenetically redistributed after deposition as indicated by the lack of a surface Mn enrichment (Figs. 3A and 4A). In a study on the effects of progressive O_2^{bw} depletion on biogeochemical processes and element fluxes in estuarine sediments, Katsev et al. (2007) have considered that a fraction of upward diffusing Mn^{2+}, which is released into the bottom water re-precipitates as hydrogenetic Mn(IV) phases. Our steady state transport-reaction model for the glacial scenario indicates that due to relatively slow reaction kinetics during the oxidation of Mn^{2+} at the oxic-suboxic boundary in the uppermost 5 cm of the sediments, a fraction of Mn^{2+} might diffuse into the bottom water (Fig. 5; Table 3). Therefore, we have adapted the recycling coefficient introduced by Katsev et al. (2007) assuming that 60% of Mn^{2+}, which diffuses into the bottom water is oxidized and re-precipitates hydrogenetically as Mn_{mobil} (Table 3). The remaining 40% of upward diffusing Mn^{2+} may accumulate onto nodules at the sediment-water interface (SWI), contributing to the nodule growth via suboxic-diagenetic accretion (e.g., Wegorzewski and Kuhn, 2014). At the BGR-RA site, comparably high Mn_{mobil} contents of 0.8 wt% at ∼ 4 cm depth are probably dominated by hydrogenetically precipitated Mn_{mobil} (Fig. 4A). The content of Mn_{mobil} may be underestimated as we have not considered the pool of Mn_{mobil} in surface nodules and buried nodules in the transport-reaction model. For the precipitation of authigenic Mn_{mobil} at the oxic-suboxic boundary in the upper few centimeters of the LGP sediments, the choice of the bioturbation coefficient becomes crucial (see Supplementary Fig. S1). Based on the transport-reaction model presented in Volz et al. (2018), we have assumed bioturbation coefficients of 0.5 cm^2 yr^{-1} for all simulated sites with logistically declining bioturbation coefficients below O_2^{bw} of 62.5 µM as suggested by Katsev et al. (2007).

Due to current Mn^{2+} upward fluxes of less than 0.04 ng Mn cm^{-2} yr^{-1}, low amounts of authigenic Mn_{mobil} precipitate at ∼ 80 cm and at 400 cm depth at the BGR-RA and IFRE-2 sites, respectively, while authigenic Mn_{mobil} is presently not precipitating at the APEI3 site due to an entirely oxic sediment column (Fig. 5; Mogollón et al., 2016; Volz et al., 2018). At lower O_2^{bw} of ∼ 100 µM, the redox boundary reaches the lowermost bioturbated layer at ∼ 7 cm depth at the BGR-RA and IFRE-2 sites with diffusive upward fluxes of Mn^{2+} at the SWI (Fig. 5; Table 3). Assuming that 40% of upward diffusing Mn^{2+} at the SWI accrete onto nodules (Katsev et al., 2007), the suboxic-diagenetic Mn^{2+} flux into the nodules is about 1.2 µg Mn cm^{-2} yr^{-1}. This Mn^{2+} flux is in the same range as the suboxic-diagenetic nodule accumulation rates

for surface nodules adjacent to the BGR-RA site, which was estimated as 2 µg Mn cm^{-2} yr^{-1} (Wegorzewski and Kuhn, 2014). Once O_2^{bw} drop below 62.5 µM, the bioturbated layer reaches oxygen levels at which bioturbation decreases (e.g., Diaz and Rosenberg, 1995; Katsev et al., 2007). Consequently, authigenic Mn_{mobil} is efficiently precipitated at the oxic-suboxic boundary in the upper few centimeters of the sediments at the BGR-RA and IFRE-2 sites (see Supplementary Fig. S1). At glacial O_2^{bw} of 35 µM, the oxic-suboxic boundary was located in the upper 5 cm of the sediments where authigenic Mn_{mobil} precipitated (Fig. 5). As expected, all Mn_{mobil} is reductively dissolved and mobilized under suboxic conditions at the IFRE-2 site, while a fraction of Mn_{mobil} remains in the sediment below the oxic-suboxic boundary at the BGR-RA site (Fig. 5). Depending on the degradability of the labile TOC fraction, it can be entirely consumed during aerobic respiration or may be further degraded during the dissimilatory reduction of Mn (oxyhydr)oxides (e.g., Froelich et al., 1979; Arndt et al., 2013). Associated with the lateral gradient of POC fluxes to the seafloor (Fig. 1; Table 1; Volz et al., 2018), the degradation coefficient for the labile TOC fraction may be higher at the BGR-RA site than at the IFRE-2 site (see Supplementary Table S1). Thus, the labile TOC fraction is completely degraded during aerobic respiration at the BGR-RA site, while Mn_{mobil} is reductively dissolved in the suboxic zone at the IFRE-2 site due to incomplete consumption of the labile TOC fraction during aerobic respiration (Fig. 5).

The LGM sediment surface was buried with sedimentation rates of 0.65 and 0.48 cm kyr^{-1} at the BGR-RA and IFRE-2 sites, respectively (Table 1; Fig. 6; Volz et al., 2018). During the enhancement of ocean ventilation during the last deglaciation (e.g., Hoogakker et al., 2018), the LGM sediment surface was located at about 3 cm depth at the BGR-RA and IFRE-2 sites (Fig. 6). As diagenetic conditions were at steady state with O_2^{bw} of 35 µM between 21-15 kyr, the Mn_{mobil} depth distribution remained the same during this time (Figs. 5 and 6). Increasing O_2^{bw} at the LGT caused the downward migration of the oxic-suboxic boundary, where only small amounts of authigenic Mn_{mobil} precipitated (Figs. 5 and 6). After the re-establishment of bioturbation during increasing sediment oxygen concentrations, the Mn_{mobil} maximum was probably mixed within the bioturbated upper 7 cm of the sediments over time (Figs. 5 and 6).

4.3. Spatial variation in sediment redox conditions during the LGP

The enrichment of authigenic U(IV) in glacial deposits at several locations throughout the Pacific further indicates that the oxic-suboxic redox boundary was located at shallow depth during glacial periods (e.g., Jaccard et al., 2009; Bradtmiller et al., 2010; Jacobel et al., 2017), and thus, reductive Fe(III) dissolution may have occurred during the LGP in some areas in the deep Pacific (e.g., Korff et al., 2016). Postulated glacial O_2^{bw} of 35 µM may have caused sediment redox conditions in CCZ allowing for the reductive dissolution of Fe(III). Bulk Fe contents (Fe$_{total}$) at the investi-
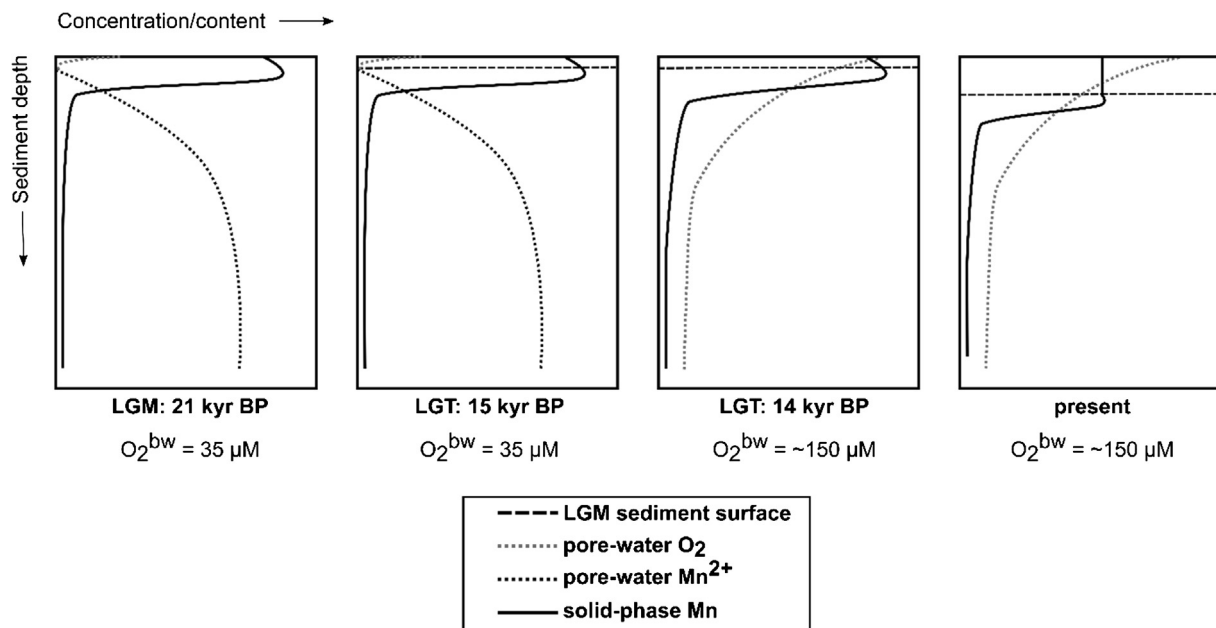
Fig. 6. Conceptual model for the depth distribution of authigenic Mn(IV) (Mn_{mobil}) since the last glacial maximum (LGM) 21 kyr before present (BP) and under current geochemical conditions in the sediments of the CCZ. During the last glacial termination (LGT) between 14-15 kyr BP, bottom-water oxygen concentrations O_2^{bw} increase from 35 μM to ∼ 150 μM within 1000 years.

gated sites are in good agreement with other studies, which have reported 4-7 wt% Fe for CCZ surface sediments (e.g., Piper, 1988). Only 30-40% of Fe_{total} are extracted during the entire combined leaching process ($Fe_{leachable}$; Fig. 3B; Table 2), while the remaining 60-70% of Fe_{total} are most likely bound to clay minerals (e.g., Rateev et al., 1969). The contents of the Fe(oxyhydr)oxide phases do not vary significantly over depth at all investigated sites with mostly constant proportions of Fe_{ox1}, Fe_{ox2} and Fe_{mag} (Fig. 4B). Thus, even with significantly lower glacial O_2^{bw}, sediment redox conditions did not go beyond Mn reduction and post-depositional Fe redistribution did most likely not occur within CCZ surface sediments. These findings are in line with the study of Heller et al. (2018) on buried CCZ nodules, which shows that Mn layers are partly dissolved while reductive mobilization of Fe upon burial did not occur.

5. Conclusion

We have studied surface sediments from six sites located in European contract areas for the exploration of polymetallic nodules within the eastern Clarion-Clipperton Zone in the NE Pacific Ocean and one site north of the CCZ in an Area of Particular Environmental Interest (APEI3). Except for the APEI3 site, all sites show solid-phase Mn maxima of up to 1 wt% in the uppermost 10 cm of the sediments. Through the application of a combined leaching protocol for the sequential extraction of mobilizable Mn (oxyhydr)oxides and various Fe (oxyhydr)oxide pools, we show that the surface sediment bulk Mn maxima are dominated (> 70%) by easily mobilizable Mn(IV). Due to oxygen penetration depths of > 0.5 m, the determined mobilizable Mn(IV) enrichments cannot have formed diagenetically under modern redox conditions. Thus, the mobilizable Mn(IV) fraction may have been formed by diagenetic relocation induced by more reducing redox conditions in the past. Lower bottom-water oxygen concentrations (O_2^{bw}) have been suggested to have prevailed basin-wide in the Pacific Ocean during the last glacial period (LGP). As a consequence, the sedimentary oxic zone was probably more condensed. Using a steady-state transport-reaction model, we demonstrate that at proposed glacial O_2^{bw} of 35 μM, the oxic-suboxic redox boundary is located

at a much shallower sediment depth than at present. Under these conditions, authigenic Mn(IV) precipitated in the upper 5 cm of the sediments, while a fraction of upward diffusing Mn^{2+} possibly contributed to the suboxic-diagenetic nodule growth. Transient transport-reaction modeling reveals that with the onset of ocean ventilation at the glacial termination, (1) the oxic-suboxic boundary shifted downward to current sediment depths, while (2) the authigenic Mn(IV) peak was mixed into subsequently depositing Holocene sediments by bioturbation. The absence of a mobilizable Mn(IV) maximum in the surface sediments of the APEI3 site indicates that the oxic zone was not as compressed during the LGP at this site due to two- to threefold lower carbon burial rates than at the sites located within the contract areas. As the APEI3 site differs significantly with respect to geochemical conditions as well as nodule size and coverage, it is not representative for the sites located in the European contract areas. Although evidence has been provided that reducing sediment redox conditions have allowed for dissimilatory Fe(III) reduction to occur at several locations in the Pacific during the LGP, our data on sequentially extracted Fe (oxyhydr)oxides indicate that Fe was not diagenetically redistributed in the sediments of our study sites.

This study represents the first baseline study on the redox cycling of Mn and Fe in deep-sea sediments of the CCZ and advances our knowledge about past changes in the oxygenation state of deep-waters of the Pacific Ocean. Our findings provide important aspects, which may improve the interpretation of Pacific sedimentary archives, and, more precisely, contribute to the long-standing discussion about the origin of Mn-rich layers widely observed in glacial deep-sea sediments.

Declaration of competing interest

The authors declare that they have no known competing financial interests or personal relationships that could have appeared to influence the work reported in this paper.

Acknowledgements

Appendix A. Supplementary material

Supplementary material related to this article can be found online at https://doi.org/10.1016/j.epsl.2019.116012.

References

Anderson, R.F., Sachs, J.P., Fleisher, M.Q., Allen, K.A., Yu, J., Koutavas, A., Jaccard, S.L., 2019. Deep-sea oxygen depletion and ocean carbon sequestration during the last ice age. Glob. Biogeochem. Cycles 33, 301–317. https://doi.org/10.1029/2018GB006049.

Arndt, S., Jørgensen, B.B., LaRowe, D.E., Middelburg, J.J., Pancost, R.D., Regnier, P., 2013. Quantifying the degradation of organic matter in marine sediments: a review and synthesis. Earth-Sci. Rev. 123, 53–86. https://doi.org/10.1016/j.earscirev.2013.02.008.

Berger, W.H., Finkel, R.C., Killingley, J.S., Marching, V., 1983. Glacial-Holocene transition in deep sea sediments: manganese spike in the east-equatorial Pacific. Nature 303, 231–233.

Boudreau, B.P., 1997. A one-dimensional model for bed-boundary layer particle exchange. J. Mar. Syst. 11, 279–303. https://doi.org/10.1016/S0924-7963(96)00127-3.

Bradtmiller, L.I., Anderson, R.F., Fleisher, M.Q., Burckle, L.H., 2006. Diatom productivity in the equatorial Pacific Ocean from the last glacial period to the present: a test of the silicic acid leakage hypothesis. Paleoceanography 21, PA4201. https://doi.org/10.1029/2006PA001282.

Bradtmiller, L.I., Anderson, R.F., Sachs, J.P., Fleisher, M.Q., 2010. A deeper respired carbon pool in the glacial equatorial Pacific Ocean. Earth Planet. Sci. Lett. 299, 417–425.

Burdige, D.J., Gieskes, J.M., 1983. A pore water/solid phase diagenetic model for manganese in marine sediments. Am. J. Sci. 283, 29–47.

Costa, K.M., Jacobel, A.W., McManus, J.F., Anderson, R.F., Winckler, G., Thiagarajan, N., 2017. Productivity patterns in the equatorial Pacific over the last 30,000 years. Glob. Biogeochem. Cycles 31 (5), 850–865. https://doi.org/10.1002/2016GB005579.

Diaz, R., Rosenberg, R., 1995. Marine benthic hypoxia: a review of its ecological effects and the behavioural response of benthic macrofauna. Oceanogr. Mar. Biol. Annu. Rev. 33, 245–303.

Finney, B.P., Lyle, M.W., Heath, G.R., 1988. Sedimentation at MANOP Site H (eastern equatorial Pacific) over the past 400,000 years: climatically induced redox variations and their effects on transition metal cycling. Paleoceanography 3, 169–189.

Froelich, P.N., Klinkhammer, G.P., Bender, M.L., Luedke, L.A., Heath, G.R., Cullen, C., Dauphin, P., Hammond, D., Hartmann, B., Maynard, V., 1979. Early oxidation of organic matter in pelagic sediments of the Eastern Equatorial Pacific, suboxic diagenesis. Geochim. Cosmochim. Acta 43, 1075–1090.

Gingele, F.X., Kasten, S., 1994. Solid-phase manganese in Southeast Atlantic sediments: implications for the paleoenvironment. Mar. Geol. 121, 317–332.

Haeckel, M., König, I., Riech, V., Weber, M.E., Suess, E., 2001. Pore water profiles and numerical modelling of biogeochemical processes in Peru Basin deep-sea sediments. Deep-Sea Res., Part 2, Top. Stud. Oceanogr. 48, 3713–3736. https://doi.org/10.1016/S0967-0645(01)00064-9.

Halbach, P., Friedrich, G., von Stackelberg, U. (Eds.), 1988. The Manganese Nodule Belt of the Pacific Ocean. Enke, Stuttgart.

Heller, C., Kuhn, T., Versteegh, G.J., Wegorzewski, A.V., Kasten, S., 2018. The geochemical behavior of metals during early diagenetic alteration of buried manganese nodules. Deep-Sea Res. Part I 142, 16–33.

Hoogakker, B.A.A., Lu, Z., Umling, N., Jones, L., Zhou, X., Rickaby, R.E.M., Thunell, R., Cartapanis, O., Galbraith, E., 2018. Glacial expansion of oxygen-depleted seawater in the eastern tropical Pacific. Nature 562 (7727), 410–413. https://doi.org/10.1038/s41586-018-0589-x.

Jaccard, S.L., Galbraith, E.D., Sigman, D.M., Haug, G.H., Francois, R., Pedersen, T.F., Dulski, P., Thierstein, H.R., 2009. Subarctic Pacific evidence for a glacial deepening of the oceanic respired carbon pool. Earth Planet. Sci. Lett. 277, 156–165. https://doi.org/10.1016/j.epsl.2008.10.017.

Jaccard, S.L., Galbraith, E.D., Martínez-García, A., Anderson, R.F., 2016. Covariation of deep Southern Ocean oxygenation and atmospheric CO2 through the last ice age. Nature 530, 207–210.

Jacobel, A.W., McManus, J.F., Anderson, R.F., Winckler, G., 2017. Repeated storage of respired carbon in the equatorial Pacific Ocean over the last three glacial cycles. Nat. Commun. 8. https://doi.org/10.1038/s41467-017-01938-x.

Katsev, S., Chaillou, G., Sundby, B., Mucci, A., 2007. Effects of progressive oxygen depletion on sediment diagenesis and fluxes: a model for the lower St. Lawrence River Estuary. Limnol. Oceanogr. 52. https://doi.org/10.4319/lo.2007.52.6.2555.

Klein, E.M., 2004. Geochemistry of the igneous oceanic crust. In: Holland, H.D., Turekian, K.K. (Eds.), Treatise on Geochemistry, Vol. 3. Elsevier, Amsterdam, pp. 433–463.

Korff, L., von Dobeneck, T., Frederichs, T., Kasten, S., Kuhn, G., Gersonde, R., Diekmann, B., 2016. Cyclic magnetite dissolution in Pleistocene sediments of the abyssal northwest Pacific Ocean: evidence for glacial oxygen depletion and carbon trapping. Paleoceanography 31, 600–624. https://doi.org/10.1002/2015PA002882.

Koschinsky, A., Fritsche, U., Winkler, A., 2001. Sequential leaching of Peru Basin surface sediment for the assessment of aged and fresh heavy metal associations and mobility. Deep-Sea Res. Part II 48, 3683–3699.

Kuhn, T., Versteegh, G.J.M., Villinger, H., Dohrmann, I., Heller, C., Koschinsky, A., Kaul, N., Ritter, S., Wegorzewski, A.V., Kasten, S., 2017. Widespread seawater circulation in 18–22 Ma oceanic crust: impact on heat flow and sediment geochemistry. Geology 45, 799–802. https://doi.org/10.1130/G39091.1.

Lutz, M.J., Caldeira, K., Dunbar, R.B., Behrenfeld, M.J., 2007. Seasonal rhythms of net primary production and particulate organic carbon flux to depth describe the efficiency of biological pump in the global ocean. J. Geophys. Res. 112, C10011. https://doi.org/10.1029/2006JC003706.

Lynn, D.C., Bonatti, E., 1965. Mobility of manganese in diagenesis of deep-sea sediments. Mar. Geol. 3, 457–474.

Mangini, A., Eisenhauer, A., Walter, P., 1990. Response of manganese in the ocean to the climatic cycles in the Quaternary. Paleoceanography 5 (5), 811–821.

Mangini, A., Jung, M., Laukenmann, S., 2001. What do we learn from peaks of uranium and of manganese in deep sea sediments? Mar. Geol. 177 (1–2), 63–78. https://doi.org/10.1016/s0025-3227(01)00124-4.

Martínez Arbizu, P., Haeckel, M., 2015. RV SONNE Fahrtbericht / Cruise Report SO239: EcoResponse Assessing the Ecology, Connectivity and Resilience of Polymetallic Nodule Field Systems, Balboa (Panama) – Manzanillo (Mexico) 11.03.-30.04.2015. https://doi.org/10.3289/GEOMAR_REP_NS_25_2015. GEOMAR Helmholtz-Zentrum für Ozeanforschung, Kiel, Germany.

Menendez, A., James, R.H., Lichtschlag, A., Connelly, D., Peel, K., 2018. Controls on the chemical composition on ferromanganese nodules in the Clarion-Clipperton Fracture Zone, eastern equatorial Pacific. Mar. Geol. 409, 1–14.

Mewes, K., Mogollón, J.M., Picard, A., Rühlemann, C., Kuhn, T., Nöthen, K., Kasten, S., 2014. Impact of depositional and biogeochemical processes on small scale variations in nodule abundance in the Clarion-Clipperton Fracture Zone. Deep-Sea Res. Part I. Oceanogr. Res. Pap. 91, 125–141. https://doi.org/10.1016/j.dsr.2014.06.001.

Mewes, K., Mogollón, J.M., Picard, A., Rühlemann, C., Eisenhauer, A., Kuhn, T., Ziebis, W., Kasten, S., 2016. Diffusive transfer of oxygen from seamount basaltic crust into overlying sediments: an example from the Clarion-Clipperton Fracture Zone. Earth Planet. Sci. Lett. 433, 215–225. https://doi.org/10.1016/j.epsl.2015.10.028.

Mogollón, J.M., Mewes, K., Kasten, S., 2016. Quantifying manganese and nitrogen cycle coupling in manganese-rich, organic carbon-starved marine sediments: examples from the Clarion-Clipperton fracture zone. Geophys. Res. Lett. 43, 2016GL069117. https://doi.org/10.1002/2016GL069117.

Perks, H.M., Charles, C.D., Keeling, R.F., 2002. Precessionally forced productivity variations across the equatorial Pacific. Paleoceanography 17, 1037. https://doi.org/10.1029/2000PA000603.

Piper, D.Z., 1988. The metal oxide fraction of pelagic sediment in the equatorial North Pacific Ocean: a source of metals in ferromanganese nodules. Geochim. Cosmochim. Acta 52, 2127–2145.

Poulton, S.W., Canfield, D.E., 2005. Development of a sequential extraction procedure for iron: implications for iron partitioning in continentally derived particulates. Chem. Geol. 214, 209–221.

Presti, M., Barbara, L., Denis, D., Schmidt, S., De Santis, L., Crosta, X., 2011. Sediment delivery and depositional patterns off Adélie Land (East Antarctica) in relation to late Quaternary climatic cycles. Mar. Geol. 284 (1–4), 96–113. https://doi.org/10.1016/j.margeo.2011.03.012.

Rapin, F., Tessier, A., Campbell, P.G., Carigan, R., 1986. Potential artifacts in the determination of metal partitioning in sediments by a sequential extraction procedure. Environ. Sci. Technol. 20, 836–840.

Rateev, M.A., Gorbunova, Z.N., Lisitzyn, A.P., Nosov, G.L., 1969. The distribution of clay minerals in the Oceans. Sedimentology 13.

Rudnick, R.L., Gao, S., 2004. Composition of the continental crust. In: Holland, H.D., Turekian, K.K. (Eds.), Treatise on Geochemistry, Vol. 3. Elsevier, Amsterdam, pp. 1–65.

Rühlemann, C., Baumann, L., Blöthe, M., Bruns, A., Eisenhauer, A., Georgens, R., Hansen, J.W., Heuer, L., Kasten, S., Kuhn, T., Martinez-Arbizu, P., Milyutina, M., Mewes, K., Picard, A., Rutkowski, J., Schott, T., Schückel, S., Schückel, U., Schwarz-Schampera, U., Tiltack, A., Utecht, C., Wohrl, C., Zoch, D., 2010. Cruise report SO-205 MANGAN, Microbiology, Paleoceanography and Biodiversity in the Manganese Nodule Belt of the equatorial Pacific, p. 248.

Thomas, E., Turekian, K.K., Wei, K.-Y., 2000. Productivity control of fine particle transport to equatorial Pacific sediment. Glob. Biogeochem. Cycles 14, 945–955.

Volz, J., Mogollón, J.M., Geibert, W., Martínez Arbizu, P., Koschinsky, A., Kasten, S., 2018. Natural spatial variability of depositional conditions, biogeochemical pro-cesses and element fluxes in sediments of the eastern Clarion-Clipperton Zone, Pacific Ocean. Deep-Sea Res. Part I 140, 159–172.

Wegorzewski, A.V., Kuhn, T., 2014. The influence of suboxic diagenesis on the formation of manganese nodules in the Clarion Clipperton nodule belt of the Pacific Ocean. Mar. Geol. 357, 123–138. https://doi.org/10.1016/j.margeo.2014.07.004.

Winckler, G., Anderson, R.F., Jaccard, S.L., Marcantonio, F., 2016. Ocean dynamics, not dust, have controlled equatorial Pacific productivity over the past 500,000 years. Proc. Natl. Acad. Sci. USA 113, 6119–6124. https://doi.org/10.1073/pnas.1600616113.

Wu, L., Wang, R., Xiao, W., Krijgsman, W., Li, Q., Ge, S., Ma, T., 2018. Late quaternary deep stratification-climate coupling in the Southern Ocean: implications for changes in abyssal carbon storage. Geochem. Geophys. Geosyst. 19 (2), 379–395. https://doi.org/10.1002/2017GC007250.